sections was studied to evaluate the distribution of haemoproteins (linked to the presence of blood vessels) and the location of the drug, respectively. For this experiment, we used DACHPt/m with diameters of 30 and 70 nm because of the critical differences in antitumour activity, tumour accumulation and microdistribution of DACHPt/m in the BxPC3 tumour model for diameters below and above 50 nm (Figs 2c,d, 3d).

In the C26 tumour model, the extensive spread of iron atoms indicates abundant vascularization (Fig. 3e), consistent with the abundance of blood vessels observed by immunofluorescence microscopy (Fig. 3b, green). DACHPt delivered from the 30 and 70 nm micelles was broadly distributed in this tumour model (Fig. 3e). In the BxPC3 xenografts, the distribution of iron atoms (Fig. 3f,g) indicates reduced vascularization and disposition of blood vessels in this model, suggesting a restricted blood flow inside the nest structures. The platinum mapping shows that the 30 nm micelles delivered DACHPt inside the cancer cell nests, whereas DACHPt from the 70 nm micelles is localized in the periphery of the nests (Fig. 3g). In both tumour models, the intratumoral microdistribution of DACHPt has a layout similar to that of the fluorescent micelles, confirming that tumour penetration by the micelles directly affects drug accumulation and antitumour outcome.

The real-time observation of *in vivo* behaviour of nanocarriers might reveal the critical barriers in a living body. Unlike conventional histological analysis, the *in vivo* confocal laser scanning microscopy (CLSM) technique enables spatiotemporal and quantitative analyses of extravasation, tissue penetration and cellular internalization of nanocarriers in a living animal[34]. By using an *in vivo* CLSM combined with a high-speed resonance scanner designed to acquire clean live tissue images, we intravitally evaluated the penetration and accumulation of the fluorescently labelled micelles. The 30 and 70 nm micelles were labelled with Alexa 488 (green) and Alexa 594 (red) fluorescent probes, respectively (Supplementary Fig. S3), and concurrently injected into tumour-bearing mice to evaluate real-time extravasation, penetration and microdistribution of both micelles in the same tumour (Fig. 4). Fluorescence measurements in the tissues were relative to the fluorescence intensity in the vasculature immediately after injection of the micelles (V_{max}).

At 1 h post-injection of the micelles, the fluorescence intensity of both 30 and 70 nm DACHPt/m in the blood vessels of tumours was ~80% of V_{max} (Fig. 4a,b). In C26 tumours, the micelles showed similar extravasation and penetration (Fig. 4a, Supplementary Video S1). The z-stack volume reconstruction of the C26 tumour showed a profusely vascularized structure and a comparable presence of both micelles in the tumour interstitium (Fig. 4c, Supplementary Video S2). In BxPC3 tumours, the extravasation profiles of the 30 and 70 nm micelles after 1 h were clearly dissimilar (Fig. 4b, Supplementary Videos S3, S4). The 30 nm micelles crossed the vascular wall, achieving over 20% of V_{max} at 40 μm from the blood vessel (Fig. 4b). In contrast, the 70 nm micelles extravasated at discrete sites close to the blood vessels and failed to move towards the interstitial space (Fig. 4b). These distinct penetration profiles were evident in the z-stack volume reconstruction of the BxPC3 tumour, showing that the extravasation points of the 70 nm micelles surrounded the blood vessels (Fig. 4d,e, Supplementary Videos S5 and S6). At 24 h post-injection, the intensities of the extravasated 30 and 70 nm micelles in the C26 tumour were ~40% of V_{max} at 100 μm from the blood vessels (Fig. 4f), and both micelles were observed inside the individual cells of the tumour tissue (Fig. 4f). In BxPC3 tumours, the distribution of the micelles corresponded reasonably to their different extravasation profiles; the 30 nm micelles achieved deep tumour accumulation, but the 70 nm micelles remained close to the vasculature (Fig. 4g, white arrows). The intensity of the extravasated 30 nm micelles was ~40% of V_{max} (Fig. 4g) and they apparently localized in the cells (Fig. 4g). These observations strongly suggest that 30 nm DACHPt/m can penetrate nests of cancer cells distant from blood vessels, allowing homogeneous drug distribution in hypopermeable tumours.

Although many factors (including morphology, hydrophobicity and nanoparticle charge) affect their accumulation in tumours, it is of primary importance to study long-circulating nanocarriers, because prolonged circulation is a prerequisite for tumour targeting based on the EPR effect. Results obtained by intratumoral microdistribution studies indicate that micellar nanomedicines with diameters less than 50 nm might be superior in terms of extravasation and penetration into tumour tissues among the sub-100 nm micellar nanomedicines. The limitation of the present study is that the size of the micellar nanomedicines was restricted to between 30 and 100 nm. Because the threshold of renal clearance of nanoparticles is ~5.5 nm (ref. 35), tumour accumulation and intratumoral distribution of nanomedicines in the range between 5 and 30 nm remain to be clarified. Furthermore, the biodistribution study revealed that the 100 nm micelles showed higher accumulation in the liver compared with other smaller micelles (Supplementary Fig. S2, Table S1), suggesting the importance of the size of nanomedicines for their distribution in organs, which may be associated with toxicity. Hence, optimizing the size of nanomedicines should take into account the balance between antitumour efficacy and potential toxicity.

Enhancing tumour permeability with a TGF-β inhibitor

We have recently reported that low doses of a transforming growth factor (TGF)-β inhibitor (TGF-β-I) transiently decreases the pericyte coverage of the endothelium in the neovasculature of pancreatic tumours, resulting in enhanced accumulation and antitumour activity of 65 nm micellar nanomedicines and 90 nm Doxil[20]. These results motivated us to evaluate the effect of the TGF-β inhibitor on the delivery of sub-100 nm DACHPt/m in BxPC3 tumours. When mice were treated with 1 mg kg^{-1} of TGF-β-I (LY364947), the 70 nm micelles reduced the tumour growth rate as effectively as the 30 nm micelles (Fig. 5a). Moreover, accumulation of the 70 nm micelles in tumours was augmented to a level comparable with that of the 30 nm micelles (Fig. 5b). These results indicate that the impaired extravasation and penetration of the 70 nm micelles in BxPC3 tumours can be overcome by treatment with TGF-β-I.

Fluorescence microscopic evaluation of BxPC3 tumour sections revealed that the fluorescently labelled 70 nm micelles showed enhanced intratumoural penetration even inside cancer cell nests after administration of TGF-β-I (Fig. 5c). This result suggests that modulation of the stromal components in tumour tissue by TGF-β-I, including pericyte coverage around the tumour blood vessels, is important for penetration of the 70 nm micelles. Moreover, the μ-SR-XRF measurement demonstrated that co-administration of TGF-β-I facilitated intratumoral delivery of DACHPt from the 70 nm micelles, which reached the interior of the cancer cell nests at 24 h post-injection (Fig. 5d). This result is consistent with the augmented antitumour activity (Fig. 5a) and enhanced intratumoural penetration (Fig. 5b) of 70 nm DACHPt/m by TGF-β-I.

Intravital CLSM observation also confirmed that treatment with TGF-β-I enhanced the extravasation and penetration of 70 nm micelles into BxPC3 tumours (Fig. 5e, Supplementary Video S7). We found that the 30 and 70 nm micelles demonstrated a comparable distribution in the tumour tissues, and both achieved ~20% of V_{max} at 40 μm from the blood vessels at 1 h after co-injection (Fig. 5e). At 24 h after injection, both micelles had deeply penetrated the tumour (Fig. 5f), reaching over 40% of V_{max} at 100 μm from the blood vessels (Fig. 5f). The 30 and 70 nm micelles also appeared to show comparable subcellular localization (Fig. 5f). These results suggest that the improvement in extravasation and penetration of 70 nm DACHPt/m by TGF-β-I caused the increased antitumour

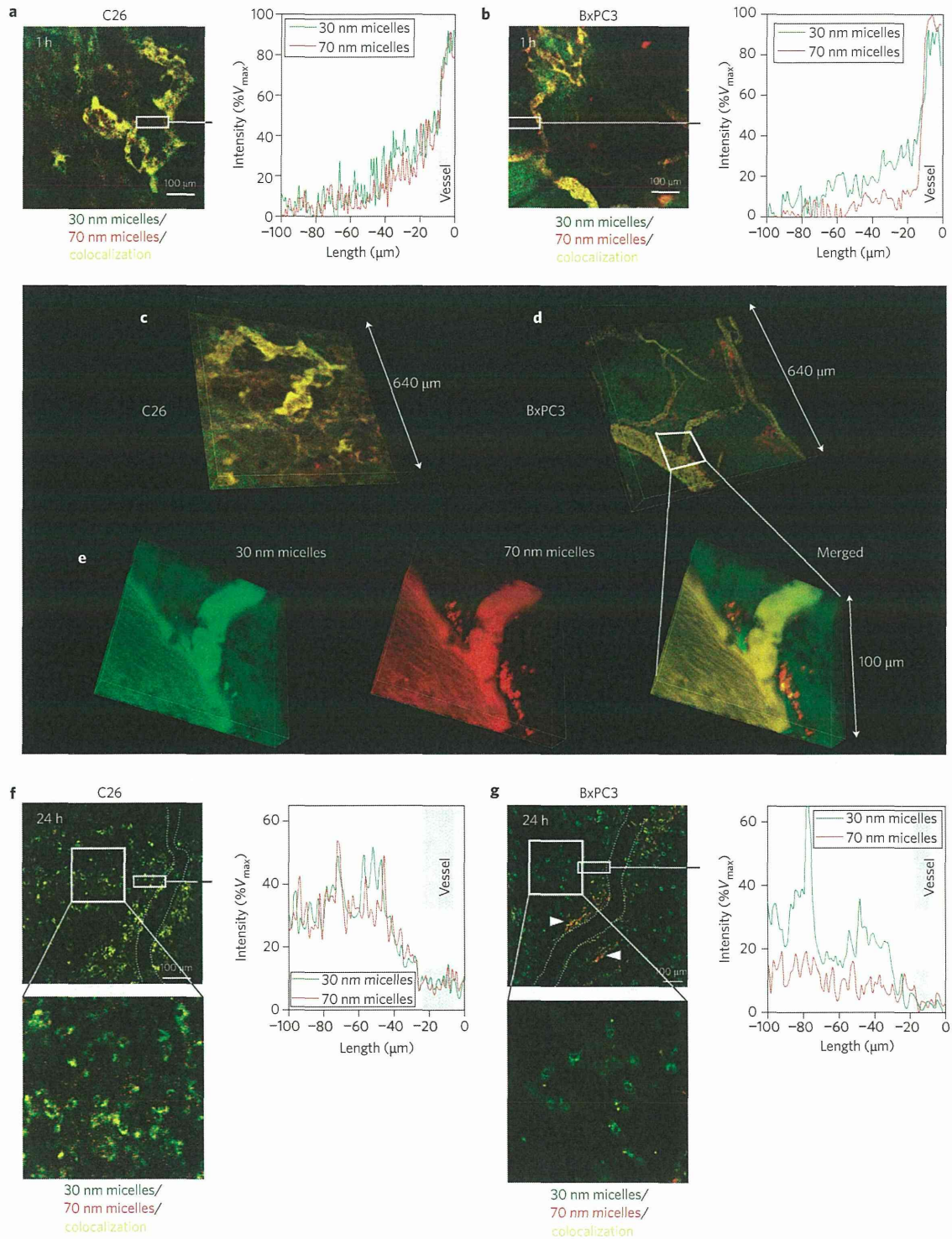

Figure 4 | *In vivo* real-time microdistribution of DACHPt/m with different diameters in tumours. a,b, Microdistribution of fluorescently labelled 30 nm (green) and 70 nm (red) micelles 1 h after injection into C26 (**a**) and BxPC3 (**b**) tumours. Their colocalization is shown in yellow. Right panels in **a** and **b** show fluorescence intensity profile from the blood vessel (0–10 μm; grey area) to the tumour tissue (10–100 μm) in the selected region (indicated by a white rectangle) expressed as a percentage of the maximum fluorescence intensity attained in the vascular region (%V_{max}). **c,d**, Z-stack volume reconstruction of C26 (**c**) and BxPC3 (**d**) tumours 1 h after co-injection of the fluorescent micelles. **e**, Magnification of the perivascular region (indicated by a white trapezium) of the z-stack volume image of BxPC3 tumours. **f,g**, Distribution of 30 and 70 nm micelles 24 h after injection into C26 tumours (**f**) and BxPC3 tumours (**g**). White arrows in **g** indicate 70 nm micelles localizing at perivascular regions. Right panels show fluorescence intensity profile from the blood vessel (0–10 μm; grey area) to the tumour tissue (10–100 μm) in the selected region (indicated by white rectangle).

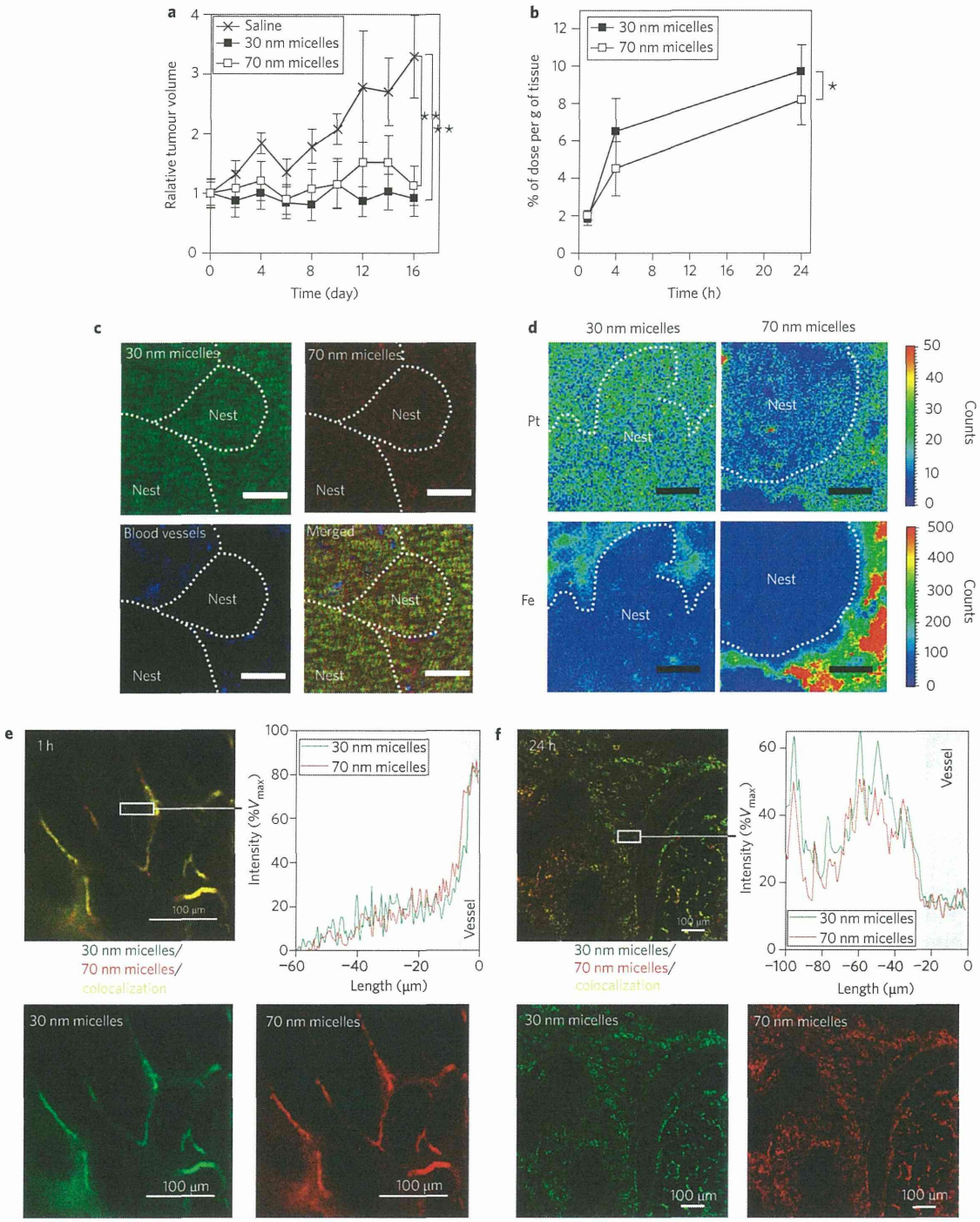

Figure 5 | Effect of TGF-β inhibitor (TGF-β-I) on antitumour activity and tumour accumulation of DACHPt/m in BxPC3 tumours. a, Graph showing relative tumour volume. Micelles (3 mg kg^{-1}) were injected on days 0, 4 and 8 and TGF-β-I on days 0, 2, 4, 6 and 8. **b**, Graph showing accumulation of 30 and 70 nm DACHPt/m in BxPC3 tumours after injection of TGF-β-I. Data are expressed as means ± s.e.m., $n = 6$. $^{*}P > 0.05$; $^{**}P < 0.01$. **c**, Fluorescent microscopy of tumour sections 24 h after co-administration of the fluorescent micelles and TGF-β-I. Scale bars, 50 μm. **d**, Platinum and iron mapping of tumour sections by μ-SR-XRF 24 h after administration of 30 and 70 nm micelles. Scale bars, 50 μm. **e**,**f**, Intravital distribution of 30 nm (green) and 70 nm (red) micelles in BxPC3 tumours 1 h (**e**) and 24 h (**f**) after co-injection of micelles and TGF-β-I. Their colocalization is shown in yellow. Right panels show fluorescence intensity profile from the blood vessel (grey area) to the tumour tissue in the selected region (indicated by a white rectangle).

activity, supporting the hypothesis that TGF-β inhibitors have great potential for enhancing the therapeutic efficacy of nanomedicines in hypopermeable tumours.

Conclusions

The enhanced targeting of drugs to cancer cells within tumours by nanomedicines largely depends on size. We have shown that the

tumoricidal efficiency of long-circulating polymeric micelles depends on the size of the micelles and the permeability of the tumour. In hypervascular tumours with a highly permeable structure, sub-100 nm micellar nanomedicines showed no size-dependent restrictions on extravasation and penetration in tumours. In contrast, only nanomedicines smaller than 50 nm can penetrate poorly permeable hypovascular tumours. Furthermore, increasing the permeability of hypovascular tumours using TGF-β signalling inhibitor improved the accumulation and distribution of the larger 70 nm micelles, offering a way to enhance the efficacy of larger nanomedicines. Because efficient extravasation and tumour penetration are important prerequisites for targeting cancer cells, our findings are important for designing sophisticated nanomedicines that are capable of cell recognition and selective intracellular release of payloads.

Materials and methods

Materials, cell lines and animals. Information regarding materials, cell lines (murine colon adenocarcinoma 26 (C26) cells and human pancreatic cancer BxPC3 cells) and animals is described in the Supplementary Information. All animal experiments were performed in accordance with the Guidelines for the Care and Use of Laboratory Animals as stated by the University of Tokyo.

Tumour models. BALB/c nude mice were inoculated subcutaneously with C26 cells (1×10^6 cell ml^{-1}) to prepare the hyperpermeable tumour model, or with BxPC3 cells (1×10^7 cell ml^{-1}) to prepare the hypopermeable tumour model. *In vivo* and *ex vivo* confocal microscopy, elemental mapping and antitumour activity studies were performed when tumours were 50 mm in volume[3]. Biodistribution studies were performed when the tumours were ~100 mm in volume[3].

Preparation of PEG–*b*-P(Glu) block copolymer and P(Glu) homopolymer. PEG–*b*-P(Glu) block copolymers and P(Glu) homopolymers were synthesized according to a previously described synthetic method[8] with a minor modification. Detailed procedures for polymer synthesis and characterization are described in the Supplementary Information. PEG–*b*-P(Glu) was fluorescently labelled by conjugating the Alexa 488 and Alexa 594 succinimidyl esters to the ω-amino group of the polymer in dimethyl sulfoxide. Detailed procedures are described in the Supplementary Information.

Preparation and characterization of DACHPt/m with different diameters. DACHPt/m with different diameters were prepared according to a previously described method with a slight modification[10,26,27]. Detailed procedures are described in the Supplementary Information. The size distribution of DACHPt/m was evaluated by DLS measurements at 25 °C, and the zeta potential of the micelles was measured in phosphate buffer at pH 7.4 using a Zetasizer Nano ZS90 (Malvern Instruments). The platinum content in the micelles was determined by ion-coupled plasma-mass spectrometry (ICP-MS) using a Hewlett Packard 4500 ICP-MS. Fluorescently labelled DACHPt/m was prepared in a similar manner with Alexa 488 or Alexa 594 labelled PEG–*b*-P(Glu). The stability of DACHPt/m with different diameters in Dulbecco's modified Eagle's medium (DMEM) containing 10% FBS at 37 °C was determined by DLS. The release rate of the micelles under similar conditions was studied by the dialysis method using a dialysis bag (molecular weight cutoff = 2,000). More detailed information is described in the Supplementary Information.

Transmission electron microscopy. The experimental procedure is described in the Supplementary Information.

***In vitro* cytotoxicity assay.** The experimental procedure is described in the Supplementary Information.

Antitumour activity assay. Mice were treated three times intravenously at two-day intervals with 3 mg kg^{-1} (on a platinum basis) of 30, 50, 70 and 100 nm DACHPt/m. Anti-tumour activity was evaluated in terms of tumour size (V), which was estimated by the equation

$$V = a \times b^2/2$$

where a and b are the major and minor axes of the tumour, respectively, as measured by a caliper. The statistical significance of different findings between the experimental and control groups was determined by analysis of variance (ANOVA) with Tukey's multiple comparison test. The results were considered statistically significant if two-tailed P-values were less than 0.05.

Plasma clearance and organ and tumour accumulation of DACHPt/m with different diameters. The experimental procedure is described in the Supplementary Information.

Microdistribution and immunohistochemistry of fluorescently labelled DACHPt/m. Mice bearing C26 or BxPC3 tumours were intravenously injected with Alexa 594-labelled 30, 50, 70 and 100 nm DACHPt/m at 100 μg per mouse on a platinum basis. Twenty-four hours later, tumours were collected and immediately frozen in an acetone/dry ice mixture. The frozen samples were further sectioned (thickness, 16 μm) in a cryostat, briefly fixed with cold acetone and then incubated with PECAM-1 antibody. Alexa 488 was used as the secondary antibody. Samples were observed using a Zeiss LSM510 Meta confocal microscope (Oberkochen). For H&E staining, the excised samples were fixed overnight in 4% paraformaldehyde and then paraffin-embedded to prepare them for the perfusion study in the tumour tissues. Samples were observed under an AX80 microscope (Olympus).

Element array analysis using μ-X-ray fluorescence. SR-XRF was used to determine DACHPt as well as iron distribution in sections of solid tumours (C26 or BxPC3) at 24 h post-intravenous injection of 30 and 70 nm DACHPt/m[36]. The detailed experimental procedure is described in the Supplementary Information.

***In vivo* confocal laser scanning microscopy (*in vivo* CLSM).** Mice bearing C26 or BxPC3 tumours were intravenously co-injected with fluorescently labelled 30 and 70 nm DACHPt/m at a dose of 10 mg kg^{-1}. The 30 nm micelles were labelled with Alexa 488, and the 70 nm micelles were labelled with Alexa 594. The *in vivo* CLSM observation of tumour tissues was performed according to a previously reported method[28,34]. All *in vivo* picture acquisitions were performed using a Nikon A1R confocal laser scanning microscope system attached to an upright ECLIPSE FN1 (Nikon). The 30-nm-diameter micelles were detected using 488/510 nm excitation/emission filters, and the signal from the 70 nm micelles was acquired with 560/620 nm excitation/emission filters.

Enhancement of tumour permeability by treatment with a TGF-β inhibitor. The effect of TGF-β inhibitor on the accumulation and antitumour activity of DACHPt/m was determined using the methods already described. For the antitumour activity experiment, BxPC3-bearing mice were administered intraperitoneal injections of TGF-β inhibitor LY364947 at 1 mg kg^{-1} every second day. For tumour accumulation studies, BxPC3-bearing mice received an intraperitoneal injection of the TGF-β inhibitor at 1 mg kg^{-1} at 1 h before co-injection of the 30 and 70 nm micelles.

Received 27 April 2011; accepted 12 September 2011; published online 23 October 2011

References

1. Duncan, R. The dawning era of polymer therapeutics. *Nature Rev. Drug Discov.* **2,** 347–360 (2003).
2. Ferrari, M. Cancer nanotechnology: opportunities and challenges. *Nature Rev. Cancer.* **5,** 161–171 (2005).
3. Torchilin, V. P. Recent advances with liposomes as pharmaceutical carriers. *Nature Rev. Drug Discov.* **4,** 145–160 (2005).
4. Davis, M. E., Chen, Z. & Shin, D. Nanoparticle therapeutics: an emerging treatment modality for cancer. *Nature Rev. Drug Discov.* **7,** 771–782 (2008).
5. Kataoka, K., Harada, A. & Nagasaki, Y. Block copolymer micelles for drug delivery: design, characterization and biological significance. *Adv. Drug Deliv. Rev.* **47,** 113–131 (2001).
6. Nishiyama, N. & Kataoka, K. Current state, achievements, and future prospects of polymeric micelles as nanocarriers for drug and gene delivery. *Pharmacol Ther.* **112,** 630–648 (2006).
7. Matsumura, Y. & Maeda, H. A new concept for macromolecular therapeutics in cancer chemotherapy: mechanism of tumouritropic accumulation of proteins and the antitumour agent SMANCS. *Cancer Res.* **46,** 6387–6392 (1986).
8. Nishiyama, N. *et al.* Novel cisplatin-incorporated polymeric micelles can eradicate solid tumours in mice. *Cancer Res.* **63,** 8977–8983 (2003).
9. Bae, Y. *et al.* Preparation and biological characterization of polymeric micelle drug carriers with intracellular pH-triggered drug release property: tumor permeability, controlled subcellular drug distribution, and enhanced *in vivo* antitumor efficacy. *Bioconjug. Chem.* **16,** 122–130 (2005).
10. Cabral, H., Nishiyama, N. & Kataoka, K. Optimization of (1,2-diamino-cyclohexane) platinum(II)-loaded polymeric micelles directed to improved tumour targeting and enhanced antitumour activity. *J. Control. Release* **121,** 146–155 (2007).
11. Maruyama, K., Ishida, O., Takizawa, T. & Moribe, K. Possibility of active targeting to tumor tissue with liposome. *Adv. Drug Deliv. Rev.* **40,** 89–102 (1999).
12. Lammers, T. *et al.* Image-guided and passively tumor-targeted polymeric nanomedicines for radiochemotherapy. *Br. J. Cancer* **99,** 900–910 (2008).
13. Matsumura, Y. & Kataoka, K. Preclinical and clinical studies of anticancer agent-incorporating polymer micelles. *Cancer Sci.* **100,** 572–579 (2009).
14. Matsumura, Y. Preclinical and clinical studies of NK012, an SN-38-incorporating polymeric micelles, which is designed based on EPR effect. *Adv. Drug Deliv. Rev.* **63,** 184–192 (2011).

15. Working, P. K. *et al.* Pharmacokinetics, biodistribution and therapeutic efficacy of doxorubicin encapsulated in stealth liposomes (DOXIL). *J. Liposome Res.* **4,** 667–687 (1994).
16. Northfelt, D. W. *et al.* Pegylated-liposomal doxorubicin versus doxorubicin, bleomycin, and vincristine in the treatment of AIDS-related Kaposi's sarcoma: results of a randomized phase III clinical trial. *J. Clin. Oncol.* **16,** 2445–2451 (1998).
17. Gradishar, W. J. *et al.* Phase III trial of nanoparticle albumin-bound paclitaxel compared with polyethylated castor oil-based paclitaxel in women with breast cancer. *J. Clin. Oncol.* **23,** 7794–7803 (2005).
18. Uster, P. S., Working, P. K. & Vaage, J. Pegylated liposomal doxorubicin (DOXIL(R), CAELYX(R)) distribution in tumour models observed with confocal laser scanning microscopy. *Int. J. Pharm.* **162,** 77–86 (1998).
19. Unezaki, S. *et al.* Direct measurement of the extravasation of polyethyleneglycol-coated liposomes into solid tumor tissue by *in vivo* fluorescence microscopy. *Int. J. Pharm.* **144,** 11–17 (1996).
20. Kano, M. R. *et al.* Improvement of cancer-targeting therapy, using nanocarriers for intractable solid tumours by inhibition of TGF-β signaling. *Proc. Natl Acad. Sci. USA* **104,** 3460–3465 (2007).
21. Dreher, M. *et al.* Tumour vascular permeability, accumulation, and penetration of macromolecular drug carriers. *J. Natl Cancer Inst.* **98,** 330–343 (2006).
22. Perrault, S. D., Walkey, C., Jennings, T., Fischer, H. C. & Chan, W. C. W. Mediating tumour targeting efficiency of nanoparticles through design. *Nano Lett.* **9,** 1909–1915 (2009).
23. Aliabadi, H. M. & Lavasanifar, A. Polymeric micelles for drug delivery. *Exp. Opin. Drug. Deliv.* **3,** 139–162 (2006).
24. Matsumura, Y. *et al.* Phase I clinical trial and pharmacokinetic evaluation of NK911, a micelle-encapsulated doxorubicin. *Br. J. Cancer* **91,** 1775–1781 (2004).
25. Plummer, R. *et al.* A phase I clinical study of cisplatin-incorporated polymeric micelles (NC-6004) in patients with solid tumours. *Br. J. Cancer* **104,** 593–598 (2011).
26. Cabral, H., Nishiyama, N., Okazaki, S., Kato, Y. & Kataoka, K. Preparation and biological properties of dichloro(1,2-diaminocyclohexane)platinum(II) (DACHPt)-loaded polymeric micelles. *J. Control. Release* **101,** 223–232 (2005).
27. Nishiyama, N. & Kataoka, K. Preparation and characterization of size-controlled polymeric micelle containing *cis*-dichlorodiammineplatinum(II) in the core. *J. Control. Release* **74,** 83–94 (2001).
28. Murakami, M. *et al.* Improving drug potency and efficacy by nanocarrier-mediated subcellular targeting. *Sci. Transl. Med.* **3,** 64ra2 (2011).
29. Alexis, F., Pridgen, E., Molnar, L. K. & Farokhzad, O. C. Factors affecting the clearance and biodistribution of polymeric nanoparticles. *Mol. Pharm.* **5,** 505–515 (2008).
30. Verma, A. *et al.* Surface-structure-regulated cell-membrane penetration by monolayer-protected nanoparticles. *Nature Mater.* **7,** 588–595 (2008).
31. Kano, M. R. *et al.* Comparison of the effects of the kinase inhibitors imatinib, sorafenib, and transforming growth factor-β receptor inhibitor on extravasation of nanoparticles from neovasculature. *Cancer Sci.* **100,** 173–180 (2009).
32. Takahashi, Y. *et al.* Significance of vessel count, vascular endothelial growth factor, and its receptor (KDR) in intestinal-type gastric cancer. *Clin. Cancer Res.* **2,** 1679–1684 (1996).
33. Sofuni, A. *et al.* Differential diagnosis of pancreatic tumours using ultrasound contrast imaging. *J. Gastroenterol.* **40,** 518–525 (2005).
34. Matsumoto, Y. *et al.* Direct and instantaneous observation of intravenously injected substances using intravital confocal micro-videography. *Biomed. Optics Exp.* **1,** 1209–1216 (2010).
35. Choi, H. S. *et al.* Renal clearance of quantum dots. *Nature Biotechnol.* **25,** 1165–1170 (2007).
36. Terada, Y. *et al.* Construction and commissioning of BL37XU at SPring-8. *AIP Conf. Proc.* **705,** 376–379 (2004).

Acknowledgements

The authors are grateful to S. Fukuda from the University of Tokyo Hospital for his valuable support in conducting transmission electron microscopy and to S. Ogura for assistance with animal care. This study was supported by the Funding Program for World-Leading Innovative R&D on Science and Technology (FIRST Program) from the Japan Society for the Promotion of Science (JSPS) and Grants-in-Aid for Scientific Research from the Japanese Ministry of Health, Labour, and Welfare. μ-SR-XRF studies were supported by the Nanotechnology Support Program of the Japan Synchrotron Radiation Research Institute (JASRI).

Author contributions

H.C. designed and performed all the experiments. Y.M. assisted with *in vivo* confocal microscopies. K.M. and Y.T. helped in the μ-X-ray fluorescence measurements. Q.C. performed transmission electron microscopy of the micelles. M.M and M.K. aided in the biodistribution experiments. H.C. wrote the manuscript. M.R.K., K.M. and M.U. commented on the manuscript. N.N. and K.K. edited the manuscript. K.K., with help from N.N., supervised the whole project.

Additional information

The authors declare no competing financial interests. Supplementary information accompanies this paper at www.nature.com/naturenanotechnology. Reprints and permission information is available online at http://www.nature.com/reprints. Correspondence and requests for materials should be addressed to N.N. and K.K.

厚生労働科学研究費補助金

第3次対がん総合戦略研究事業

新戦略に基づく抗がん剤の開発に関する研究

平成22年度~25年度　総合研究報告書

研究代表者　　松村保広（平成22年度~24年度）

安永正浩（平成25年度）

平成26(2014)年　3月

2/2冊

目　　次

Ultrasound-mediated Transfection with Liposomal Bubbles Delivers Plasmid DNA Directly into Nucleus

Takeshi Kawazu,[1] Kazumi Hakamada,[2] Yusuke Oda,[3] Jun Miyake,[2] Kazuo Maruyama,[3] and Takeshi Nagasaki*[1]

[1]*Department of Applied Chemistry and Bioengineering, Graduate School of Engineering, Osaka City University, 3-3-138 Sumiyoshi-ku, Osaka 558-8585*

[2]*Department of Mechanical Science and Bioengineering, Graduate School of Engineering Science, Osaka University, 1-3 Machikaneyama, Toyonaka, Osaka 560-8531*

[3]*Department of Biopharmaceutics, School of Pharmaceutical Sciences, Teikyo University, 1091-1 Suwarashi, Sagamiko, Sagamihara, Kanagawa 229-0195*

(Received January 5, 2011; CL-110002; E-mail: nagasaki@bioa.eng.osaka-cu.ac.jp)

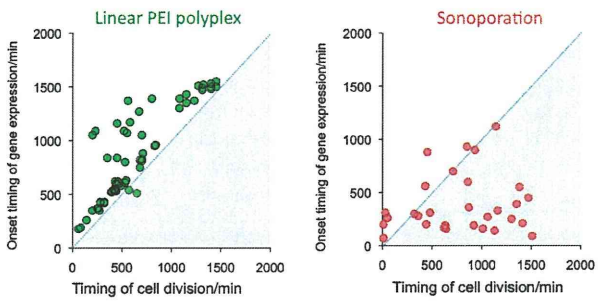

REPRINTED FROM

Chemistry Letters

Vol.40 No.3 2011 p.298–299

CMLTAG

March 5, 2011

The Chemical Society of Japan

Published on the web February 16, 2011; doi:10.1246/cl.2011.298

doi:10.1246/cl.2011.298
Published on the web February 16, 2011

Ultrasound-mediated Transfection with Liposomal Bubbles Delivers Plasmid DNA Directly into Nucleus

Takeshi Kawazu,[1] Kazumi Hakamada,[2] Yusuke Oda,[3] Jun Miyake,[2] Kazuo Maruyama,[3] and Takeshi Nagasaki*[1]
[1]*Department of Applied Chemistry and Bioengineering, Graduate School of Engineering, Osaka City University, 3-3-138 Sumiyoshi-ku, Osaka 558-8585*
[2]*Department of Mechanical Science and Bioengineering, Graduate School of Engineering Science, Osaka University, 1-3 Machikaneyama, Toyonaka, Osaka 560-8531*
[3]*Department of Biopharmaceutics, School of Pharmaceutical Sciences, Teikyo University, 1091-1 Suwarashi, Sagamiko, Sagamihara, Kanagawa 229-0195*

(Received January 5, 2011; CL-110002; E-mail: nagasaki@bioa.eng.osaka-cu.ac.jp)

Transfection using ultrasound exposure in the presence of nanobubbles can overcome an important barrier for nonviral gene delivery, that is entering the nucleus without cell division. The monitoring of the relationship between fluorescent protein expression and cell division reveals that ultrasound-mediated transfection with liposomal bubbles is independent on the disappearance of nuclear membrane at mitosis.

In many cases, nonviral gene transfer depends on the cell cycle.[1] Giorgio et al. found that mitosis enhances transgene expression of plasmid DNA delivered by cationic liposomes.[2] The critical rate-determining step for nonviral gene delivery is nuclear entry of an exogenous gene.[3] Although enormous efforts have been directed to this problem, an estimation method has not been established for a long time.[4] Recently Hakamada, Miyake, and co-worker reported the examination of cell morphology and the dynamics of EGFP gene expression by using a fluorescent microscopic apparatus capable of monitoring single cell behavior.[5] With a lipoplex (Lipofectamine LTX, Invitrogen, Carlsbad, CA, USA) as nonviral vector, their results definitely showed that the onset timing of gene expression depended on cell division. This work semiquantitatively demonstrates for the first time that the nuclear envelope determines the rate of nonviral gene delivery.

On the other hand, it is well known that physical methods such as electroporation and sonoporation are effective gene-delivery methods especially for primary cells.[6] Wagner et al. reported that gene transfer by electroporation shows hardly any cell cycle dependence.[7] Maruyama et al. succeeded in the enhancement of sonoporation transfection efficiency by combining ultrasound and acoustic liposomes (bubble liposomes) which contain the ultrasound imaging gas perfluoropropane.[8] Bubble liposomes could act as an effective gene-delivery tool not only in vitro but also in vivo.[9] Under ultrasound exposure, the cavitation of nanobubbles in liposomes induced mechanical constraints on the plasma membrane and increased the membrane permeability by the creation of nanosize pores. The kinetics of protein expression was significantly faster for sonoporation than for lipofection that requires endocytosis.[10] However, very little is known whether ultrasound affects plasmid entry into the nucleus. In this paper, cell division and protein expression kinetics on ultrasound-mediated gene delivery with bubble liposomes have been studied by Hakamada's method.[5]

In 24-well culture plate, NIH3T3 cells (mouse fibroblast) were seeded at 6×10^4 cells per well and cultured at 37 °C with 5% CO_2 atmosphere in 10% FBS-containing DMEM. Cells were transfected with pCMV-Venus encoding a green fluorescent protein (venus) under the control of the CMV promoter. After transfection, phase-contrast and fluorescent images of cells in each well were recorded at intervals of 10 min for 30 h, and their exposure times were 50 and 400 ms, respectively. The measurement was started at 1 h post-transfection. As a compared nonviral gene carrier, linear poly(ethyleneimine)s (jetPEI, Polyplus-Transfection, Illkirch, France) was used because it showed high transfection ability in vitro and in vivo.[11] The transfection procedure was followed with manufacturer's instruction. On the other hand, preparation of bubble liposomes and transfection of plasmid DNA using bubble liposomes are carried out according to similar way previously reported by Maruyama et al.[8b] The ultrasound was exposed for 10 s under following conditions: frequency, 2 MHz, duty, 50%; intensity, 2.5 W cm^{-2}; burst rate, 2 Hz using Sonopore 3000 (NEPA GENE, CO., LTD., Chiba, Japan).

The results of jetPEI (Figure 1a) show a similar relationship between the timing of cell division and the onset timing of gene expression as that by lipofection.[5] The peak of protein expressing cells appeared around 10 h post-transfection

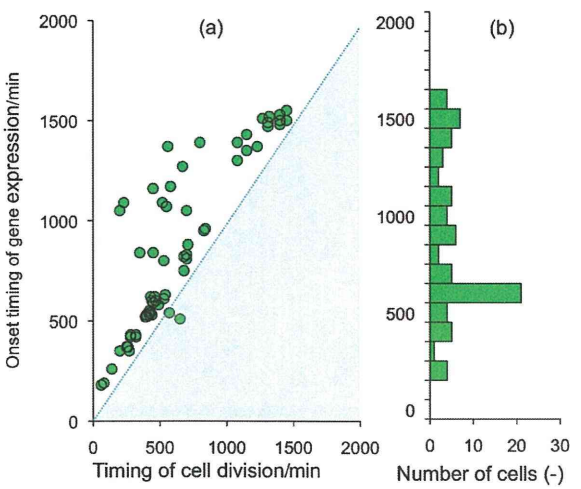

Figure 1. (a) Correlation between the timing of cell division and the onset of protein expression by jetPEI-mediated transfection. (b) Distribution of the cell number on the onset timing on jetPEI-mediated transfection.